J. Fluid Mech. (2007), *vol.* 576, *pp.* 377–403. © 2007 Cambridge University Press
doi:10.1017/S0022112007004648 Printed in the United Kingdom

On impulsively generated inviscid axisymmetric surface jets, waves and drops

K. K. TJAN AND W. R. C. PHILLIPS

Department of Theoretical and Applied Mechanics,
University of Illinois at Urbana-Champaign, Urbana, IL 61801-2935, USA
ktjan@engineering.uiuc.edu;wrphilli@uiuc.edu

(Received 20 April 2006 and in revised form 16 October)

The evolution of an unbounded inviscid free surface subjected to a velocity potential of Gaussian form and also to the influence of inertial, interfacial and gravitational forces is considered. This construct was motivated by the occurrence of lung haemorrhage resulting from ultrasonic imaging and pursues the notion that bursts of ultrasound act to expel droplets that puncture the soft air-filled sacs in the lung plural surface, allowing them to fill with blood. The tissue adjacent to the sacs is modelled as a liquid and the air–tissue interface in the sacs as a free surface. The evolution of the free surface is described by a boundary-integral formulation and, since the free surface evolves slowly relative to the bursts of ultrasound, they are realized as an impulse at the free surface, represented by the velocity potential. As the free surface evolves, it is seen to form axisymmetric surface jets, waves or droplets, depending upon the levels of gravity and surface tension. Moreover the droplets may be spherical and ejected away from the surface or an inverted tear shape and fall back to the surface. These conclusions are expressed in a phase diagram of inverse Froude number Fr^{-1} versus inverse Weber number We^{-1}. Specifically, while axisymmetric surface jets form in the absence of surface tension and gravity, gravity acts to bound their height, rendering them waves, although instability overrides the calculation prior to its reaching that bound. Surface tension acts to suppress the instability (provided that $We^{-1} > 0.045$) and to form drops; if sufficiently strong it can also damp the evolving wave, causing it to collapse. The pinchoff which effects spherical drops is of power-law type with exponent 2/3, and the universal constant that relates the necking radius to the time from pinchoff, thereby realizing a finite-time singularity, has the value $\mathfrak{K} = 0.45 \pm 0.025$. Finally, drops can occur once the mechanical index, a dimensional measure used in ultrasonography, exceeds 0.5.

1. Introduction

Ultrasonic imaging has long been a standard procedure in clinical medicine. It is popular because of its ease of use and the insight it provides, with no documented health risks or side effects. Yet the safety of ultrasonography has lately come under scrutiny following the publication of experimental results reporting lung hemorrhage in animals exposed to ultrasound at acoustic-pressure levels typical of human diagnostics. The animals include mice (Child *et al.* 1990), monkeys (Tarantal & Canfield 1994), rabbits (Zachary & O'Brien 1995), pigs (Harrison *et al.* 1995) and rats (Holland *et al.* 1996). Mechanisms suggested to explain these observations are broadly classified into thermal and non-thermal, the non-thermal mechanisms being

https://doi.org/10.1017/S0022112007004648 Published online by Cambridge University Press

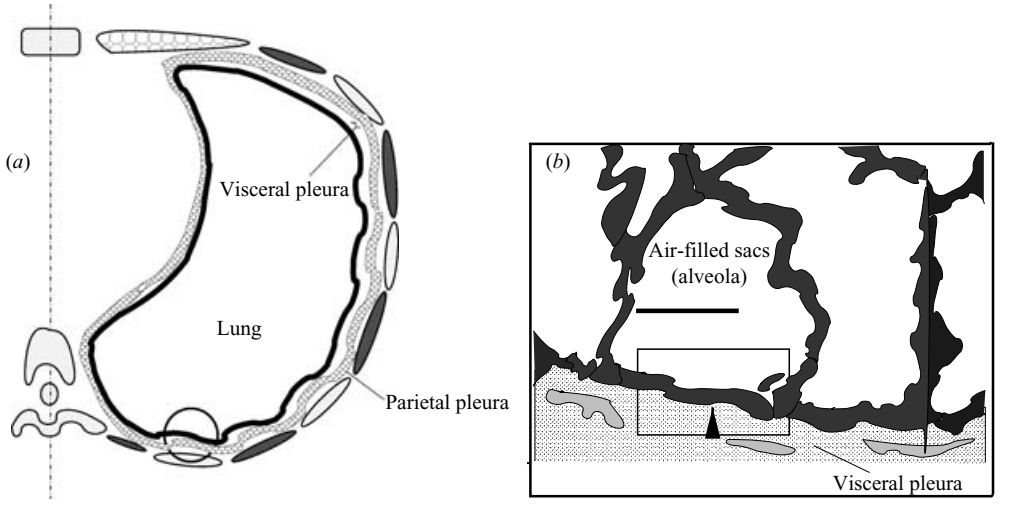


FIGURE 1. Diagrams of the lung: (*a*) a cross-section through the chest showing the pleural cavity and lung. The region of the circle in (*a*) is shown larger in (*b*), which is a schematic photomicrograph illustrating the anatomy of the visceral pleura and contiguous septa. The arrow denotes the direction of acoustic propagation. The box shows the air–blood barrier at the interface of tissue and air modelled herein. The horizontal bar is of length 100 μm. The walls separating the alveola are several hundred nanometres thick and are not drawn to scale.

further broken down into cavitation-induced and non-cavitation-induced mechanisms. Studies by Child *et al.* (1990) and Hartman *et al.* (1990), however, indicate that thermal effects are not likely to be responsible for lung hemorrhage; accordingly extensive experiments by Zachary *et al.* (2000*b*) led to the conclusion that lung hemorrhage is not caused by inertial cavitation. The purpose of the present work, therefore, is to explore a plausible non-cavitational damage mechanism.

The mechanism we consider is built around the notion that ultrasound focused near a tissue–liquid interface acts to expel tiny droplets (of blood or an other fluid), which then puncture the soft bubble-wrap-like sacs of the lung pleural surface, allowing them to fill with blood. The knowledge that droplets are emitted from an acoustically excited air–liquid interface dates from Wood & Loomis (1927), who reported the formation of a fog of droplets on the surface of thin liquid films subjected to ultrasound. Lang (1962) subsequently conducted a similar set of experiments on both liquid films and deeper liquid pools, observing the formation of fine dense fog when the film is continuously excited by ultrasound in the frequency range 10–800 kHz. More recently, Elrod *et al.* (1989) reported the use of a high-intensity focused acoustic beam to eject isolated droplets from the free surface of a liquid, using ultrasonic transducers operating over the range 5–300 MHz, which includes the operating frequencies of ultrasonic medical devices (2–12 MHz). Furthermore, rather than applying continuous forcing as used previously, these authors used bursts (often denoted tone bursts) of focused ultrasound in an effort to expel single droplets, relevant to inkjet printing. Tone bursts of focused ultrasound are also used in diagnostic ultrasonography.

The lung lives in the pleural cavity and grows to fill it, as shown in figure 1(*a*), and encasing the lung is a single-celled membrane called the pleura, composed of two layers, the visceral pleura immediately adjacent to the lung and then the parietal

https://doi.org/10.1017/S0022112007004648 Published online by Cambridge University Press

pleura. At the surface of the lung, alveolar septa anatomose with the visceral pleura to form a collection of air-filled sacs (alveoli), seen in figure 1(*b*), the linings of which form the air-blood barrier. The thickness of this barrier in a human being is about 750 nm (Zachary *et al.* 2000*a*). Together these layers form the pleural surface, the cross-section of which resembles foam or bubble wrap. Thus, since human tissue is largely composed of liquid, albeit in a congealed form, and since sacs in the lung pleural surface are gas filled and adjacent to a gas cavity, our simplistic metaphor for the chest encasing the lung is a liquid, while that for the pleural-surface–air interface of the lung is the free surface of the liquid.

Consider then a Newtonian liquid in which ultrasound (from an immersed transducer whose axis of symmetry is normal to the free surface) is brought to a focus near the free surface. Our task is to question under what conditions bursts of ultrasound eject drops from the free surface and to view those findings in the context of haemorrhage at the lung surface. However, in doing so we shall not restrict our study solely to conditions associated with lung haemorrhage but rather look in general at impulsively generated waves and drops.

Multiple time scales enter the problem: the shortest one, T_λ say, characteristic of the period of the ultrasound (about 0.3 μs); a second, T_b, indicative of the tone burst (about $20T_\lambda$–$50T_\lambda$); and a much longer one, T, representative of the evolution of the free surface (about 0.1 s). Thus while $T_\lambda \leqslant T_b$ always, of interest here is the situation $T_\lambda \ll T_b$, such that $T_\lambda \ll T_b \ll T$. Events that occur over a time T_b are then, in relation to T, essentially averaged over T_b. Thus harmonic fluctuations from the transducer vanish, but quadratic wave–wave (or higher) nonlinearities remain; moreover, since $T_b \ll T$, they are felt on the time scale T as an impulse in pressure that sets the system into motion. Likewise, while the substrate is necessarily compressible to harmonic inputs on the time scale of the ultrasound, it is incompressible from the T_b-averaged viewpoint of the evolving free surface.

The ultrasound is focused, not to a point but rather to a zone whose length scale $L = \mathfrak{h}\lambda$ is, at a minimum, of the order of the wavelength λ of the ultrasound (about 500 μm), implying that the constant $\mathfrak{h} \geqslant O(1)$. L is thus vastly smaller than the overall size of the lungs albeit larger than individual sacs in the pleural surface. However, since the walls of the sacs are only several hundred nanometres thick, they will not obstruct the ultrasound; indeed the ultrasound sees only an unbounded region of gas. Thus from the viewpoint of our construct, and since the impulse is radially symmetric, we pose the initial-value problem as being in an unbounded axisymmetric domain.

Surface tension is likely to play a key role in the formation of droplets, and gravity also, but the role of viscosity is less clear. We may grant that the pinchoff process to individual drops is viscous, but the absence of a solid boundary and the impulsive nature of the problem are more indicative of an inviscid evolution to the point of pinchoff. To pursue this further we note that, were viscous terms to be retained in the equation of motion, they would scale, relative to the curvature terms, as $We/Re = (\nu^2\rho/\mathfrak{h}\lambda\sigma)^{1/2}We^{1/2}$. Here Re is the Reynolds number, defined using the length and velocity scales to be introduced with the Weber number We in § 2.2, and ν is the kinematic viscosity (the other symbols are defined later). It readily follows that $We/Re \ll 1$, in support of an inviscid model.

Finally, in the absence of a rigid boundary and in the absence of buoyancy, there is no way to create or diffuse vorticity and hence the fluid remains irrotational. In consequence we investigate impulsively generated axisymmetric jets, waves and drops from the free surface of an unbounded inviscid irrotational liquid subject to the interplay of inertial, interfacial and gravitational forces.

https://doi.org/10.1017/S0022112007004648 Published online by Cambridge University Press

Little attention has been paid to nonlinear axisymmetric standing waves at a free surface, although Cinbis, Mansour & Khuri-Yakub (1993) considered them with a view to measuring surface tension and numerical techniques to handle them date from Dommermuth & Yue (1987).

Drop formation, however, has received considerable attention, albeit drops induced by gravitational or periodic accelerative forcing over length scales which are fixed or periodic. Examples include viscous dripping (Wikes, Phillips & Basaran 1999; Brenner *et al.* 1997) and liquid-jet breakup (Lin & Reitz 1998), where the geometry of the exit nozzle imposes a length scale for the problem. Vibration may also stimulate the formation of droplets through parametric excitation (Faraday 1831). Here too the domain is finite and although the forcing is time periodic, it is continuous and at frequencies well below those of ultrasound (see e.g. James, Smith & Glezer 2003). These constructs are vastly different from ours and we expect the dynamics which effect droplet formation to likewise differ, although not the details of the capillary pinchoff of the drop. Indeed, capillary pinchoff is likely to be found in all studies. Pinchoff has been studied on its own (by e.g. Eggers 1993; Brenner, Lister & Stone 1996; Monika & Stee 2004) and in the context of ink-jet printing (by e.g. Day, Hinch & Lister 1998; Basaran 2002; Leppinen & Lister 2003).

The only study concerned with impulsively generated drops on an unbounded domain would appear to be that of Elrod *et al.* (1989), which includes both experiments and modelling. These authors approached the topic from the viewpoint of inkjet printing and began by constructing a simple theory to relate, *inter alia*, the diameter and the initial velocity of the drop to the ultrasound frequency. They then developed a more elaborate numerical model that predicts the actual time evolution of the surface. In this model they ignored gravity and introduced a scaling that leaves the governing equations devoid of parameters. This means that solutions for intensity profiles of the same shape can be scaled according to the magnitude of the intensity. Their findings compare well with experiment.

But such a scaling requires that Φ, which measures the strength of the impluse (see §§2.2 and 5.3 below), should scale with the square root of the surface tougent σ, whereas we would like to fix Φ and vary σ. We are also interested in the role of gravity. For that reason we work with a non-canonical two-parameter set, namely a Weber number We (that captures σ) and a Froude number Fr that includes gravity; for precise definitions see §2.2. We can then investigate the zero-gravity no-surface-tension double limit, $We^{-1} \to 0$, $Fr^{-1} \to 0$ (§4.1); the single limits $We^{-1} \to 0$, $Fr^{-1} \neq 0$ (§4.2), $We^{-1} \neq 0$, $Fr^{-1} \to 0$, the latter of which which recovers Elrod *et al.* (1989) (§4.3); and the two-parameter set $We^{-1} \neq 0$, $Fr^{-1} \neq 0$ (§4.4).

Our problem involves solving the Laplace equation (2.1) subject to the Bernoulli equation (2.2) on the free surface. Equation (2.1) is best recast into a boundary-integral form and we do so in §2.3 in a manner akin to that of Baker, Meiron & Orszag (1984). This technique has been recently employed by others (*e.g.* Hou, Lowengrub & Shelley 1994, 1997, 2001; Nie & Baker 1998; Nie 2001); but because their work is formulated in either a finite or periodic domain, it cannot be readily adapted to our problem, which lives on an unbounded domain. Moreover, while the evolution of the free surface is monitored through a single variable (the surface-tangent angle) in their problems, for reasons explained in §3.2 it is best that we monitor two variables, the radius and elevation. This we do in the manner of Lundgren & Mansour (1988). Of course for numerical reasons it is desirable that we too work on a finite domain and for that reason we construct an invertible mapping to a finite domain (see §3.1) which yields the appropriate asymptotic behaviour of the solutions, a feature we investigate

https://doi.org/10.1017/S0022112007004648 Published online by Cambridge University Press

in § 2.5. Our method for computing numerical derivatives of the surface and thus of the surface curvature, which is crucial to numerical stability, is outlined in § 3.2. Results are given in § 4, followed in § 5.1 by a discussion of the finite-time singularity which occurs at pinchoff. Critical *We* (Weber number) numbers and what they mean *vis à vis* lung haemorrhage are discussed in § § 5.2 and 5.3.

2. Formulation and analysis

2.1. *Governing equation*

We consider an axisymmetric fluid domain $\mathfrak{D}^*$ ($r^*[0, \infty), z^*(-\infty, \infty)$), which contains an inviscid incompressible liquid of density ρ. Gravity g acts in the negative z^* direction and the free surface, which we identify as $\mathscr{S}$, is initially located at $z^* = 0$. The coefficient of surface tension on $\mathscr{S}$ is σ. Of interest is how the free surface evolves when $\mathfrak{D}^*$ is subjected to a spatially dependent impulse at time $t^* = 0$.

We assume, *ab initio*, that the fluid is irrotational; this permits a velocity potential φ^* in $\mathfrak{D}^*$ to be defined in terms of the velocity vector $\boldsymbol{u}^* = \nabla^* \varphi^*$, while incompressibility $\nabla^* \cdot \boldsymbol{u}^* = 0$ demands that φ^* satisfy the Laplace equation

$$\nabla^{*2} \varphi^*(\boldsymbol{r}^*) = 0, \qquad \text{where} \quad \boldsymbol{r}^*(r^*, z^*) \in \mathfrak{D}^*. \tag{2.1}$$

In such circumstances, and under conservative body forces, the momentum equations reduce to the unsteady Bernoulli equation,

$$\frac{\partial \varphi^*}{\partial t^*} + \frac{1}{2} \boldsymbol{u}^* \cdot \boldsymbol{u}^* + \frac{p^*}{\rho} + g z^* = 0 \qquad \text{where} \quad \boldsymbol{r}^*(r^*, z^*) \in \mathfrak{D}^*, \tag{2.2}$$

which gives an explicit expression for the pressure p^* at any point in $\mathfrak{D}^*$.

The initial-value problem is completed by a boundary condition which requires for all t^* that $\boldsymbol{u}^*$ vanish at infinity. Two further boundary conditions apply on the interface $\mathscr{S}$ a kinematic condition which requires that the velocity normal to the fluid surface be identical to that of the fluid particle at the surface, i.e. that the surface be a material surface; and a dynamic condition which requires that the pressure on $\mathscr{S}$ be constant. With no loss we set this constant to zero and utilize it in the Laplace–Young condition (Young 1805), which requires that surface tension balance the pressure difference across the interface; (2.2) then becomes

$$\frac{\partial \varphi^*}{\partial t^*} + \frac{1}{2} \boldsymbol{u}^* \cdot \boldsymbol{u}^* + \frac{\sigma}{\rho} \kappa^* + g z^* = 0 \quad \text{on} \quad \mathscr{S}, \tag{2.3}$$

where κ^* is the mean curvature of $\mathscr{S}$; in the meridional direction this is κ_r^* and in the azimuthal direction it is κ_ϑ^* (see (3.3) below). Our task is to monitor the evolution of $\mathscr{S}$ when the the fluid is impulsively set into motion by the imposition of an initial velocity potential $\varphi_0^* = \varphi^*(r^*, z^*, t^*)|_{t^*=0}$ throughout $\mathfrak{D}^*$.

2.2. *Non-dimensionalization*

Since the fluid domain is unbounded the geometry presents no natural length scales. However, time and length scales are introduced by the initial velocity potential φ_0^* imposed on the system, where $\Phi = \varphi_0^*|_{max}$, say, characterizes the strength and L the spatial extent of φ_0^*. Then, since Φ has the dimension of length squared per unit time, the time scale T follows as $T \equiv L^2/\Phi$, with velocity scale ΦL^{-1}, allowing us to write $r^* = Lr$, $z^* = Lz$, $\kappa^* = L^{-1}\kappa$, $\varphi^* = \Phi\varphi$, $t^* = Tt$ and $\boldsymbol{u}^* = \Phi L^{-1} \boldsymbol{u}$, where r, z, κ, ϕ, t and $\boldsymbol{u}$ are dimensionless quantities. Finally, we note that $\varphi_0^* \propto p^*/f$ where f is the acoustic frequency (see § 5.3).

https://doi.org/10.1017/S0022112007004648 Published online by Cambridge University Press

Equation (2.3) then becomes

$$\frac{\partial \varphi}{\partial t} + \frac{1}{2}\boldsymbol{u}\cdot\boldsymbol{u} + \frac{\kappa}{We} + \frac{z}{Fr} = 0. \tag{2.4}$$

Two dimensionless groups are evident in (2.4), the Weber number, $We = \Phi^2\rho(L\sigma)^{-1}$, which measures the relative importance of inertial and interfacial forces, and the Froude number $Fr = \Phi^2/(gL^3)$, which measures the relative importance of inertial and gravitational forces. Fr may further be written as We/Bo, where the Bond number $Bo = \rho g L^2/\sigma$ measures the ratio of gravitational and surface-tension forces.

2.3. *Boundary integral equation*

Since our main interest is in the evolution of the surface $\mathscr{S}$, a computationally efficient way to solve (2.1) subject to the initial and boundary conditions is through a boundary-integral formulation. In such a formulation, a volume integral over the solution domain $\mathfrak{D}$ is converted into a surface integral and the dimensionality of the problem is reduced by one, to wit $\varphi(r, z, t) \mapsto \phi(s, t)$, where s is the arc length along Γ, the curve which describes $\mathscr{S}$ in the (r, z)-plane, with $r = r(s)$ and $z = z(s)$.

In constructing this mapping we first note that the fundamental solution to the Laplace equation (2.1) is the Green's function $\mathscr{G}(\boldsymbol{r}|\boldsymbol{r}') = -(4\pi|\boldsymbol{r} - \boldsymbol{r}'|)^{-1}$. Here $\boldsymbol{r} = (r, z, \theta)$, where r and z are defined above and θ is the azimuthal angle, measured anticlockwise in the (r, z)-plane. We next note from classical results in potential theory (see e.g. Jaswon & Symm 1977) that ϕ may be expressed as a distribution of dipoles of strength μ along the surface Γ.

When written in this form, the potential ϕ satisfies the Laplace equation everywhere except at the source point $\boldsymbol{r}'$ and is discontinuous across the line Γ. Nevertheless, we may use the Plemelj formula to define ϕ on Γ as the value in the limit as $\boldsymbol{r}$ tends to Γ from within $\mathfrak{D}$. However, the integrand is now singular at the point $\boldsymbol{r} = \boldsymbol{r}'$, rendering the integral a principal-value integral (denoted $\fint$). For numerical reasons it is best to 'desingularize' the integrand and to that end we subtract a complementary principal-value integral which can be evaluated analytically. We then find that

$$\phi(\boldsymbol{r}) = \frac{1}{2}\mu(\boldsymbol{r}) + \fint_{\Gamma} [\mu(\boldsymbol{r}') - \mu(\boldsymbol{r})]\boldsymbol{n}'\cdot\nabla_{\boldsymbol{r}'}\mathscr{G}(\boldsymbol{r}|\boldsymbol{r}')\,\mathrm{d}\Gamma', \tag{2.5}$$

which is a Fredholm integral equation of the second kind; $\boldsymbol{n}$ is the unit outward normal and primes denotes quantities that vary with the integration variable.

Since the problem is posed in an axisymmetric domain, we can make further progress analytically by calculating the azimuthal contribution to the integral. We proceed by first writing $\mathrm{d}\Gamma'$ as $r'\,\mathrm{d}\theta'\,\mathrm{d}s'$, where s is the surface arclength measured radially outwards from $r = 0$. Axisymmetry then demands that both ϕ and μ be functions solely of s, which allows us to factor $\mu(s') - \mu(s)$ out from the azimuthal integral, so that

$$\phi(s) = \frac{1}{2}\mu(s) + \fint_{0}^{\infty} [\mu(s') - \mu(s)]\mathscr{K}_{\phi}(s|s')\,\mathrm{d}s', \tag{2.6}$$

where

$$\mathscr{K}_{\phi}(s|s') = \int_{0}^{2\pi} \boldsymbol{n}'\cdot\nabla_{\boldsymbol{r}'}\mathscr{G}(\boldsymbol{r}|\boldsymbol{r}')r'\,\mathrm{d}\theta'.$$

https://doi.org/10.1017/S0022112007004648 Published online by Cambridge University Press

Of course we must still evaluate $\mathscr{K}_\phi$. To do so we first express $\boldsymbol{r}$ and $\boldsymbol{n}$ in Cartesian coordinates as

$$\boldsymbol{r} = \begin{pmatrix} r\cos\theta \\ r\sin\theta \\ z \end{pmatrix} \quad \text{and} \quad \boldsymbol{n} = \begin{pmatrix} n_r\cos\theta \\ n_r\sin\theta \\ n_z \end{pmatrix},$$

where n_r and n_z are the radial and vertical components of the unit outward normals; $\mathscr{K}_\phi$ then becomes

$$\mathscr{K}_\phi(s|s') = \frac{r'}{\pi A^3}\left\{(r'n_r' - (z-z')n_z')\frac{E(k)}{1-k} + \frac{rn_r'}{k}\left[\frac{2-k}{1-k}E(k) - 2K(k)\right]\right\},$$

where $A = \sqrt{(r+r')^2 + (z-z')^2}$ and $k = 4rr'A^{-2}$. Here $K(k)$ and $E(k)$ refer respectively to complete elliptic integrals of the first and second kind. It is also understood that r and z are functions of s while r', z', r_r' and n_z' are functions of s'.

The formulation is now complete. However, for numerical implementation it is convenient to work with both the velocity potential ϕ and the pseudo-streamfunction ψ (Lundgren & Mansour 1988). This allows us to compute the normal velocity u_n at the surface by taking the surface derivative of ψ rather than the normal derivative of ϕ.

An expression for the pseudo-streamfunction ψ can be obtained by writing $\boldsymbol{u} = \nabla \times \boldsymbol{B}$ and considering the associated vector potential $\boldsymbol{B} = (B_r, B_\theta, B_z)$ as

$$\boldsymbol{B}(\boldsymbol{r}) = -\fint_\Gamma \mu(\boldsymbol{r}')\boldsymbol{n}' \times \nabla_{\boldsymbol{r}'}\mathscr{G}(\boldsymbol{r}|\boldsymbol{r}')\,\mathrm{d}\Gamma' \quad \boldsymbol{r} \in \Gamma,\ \boldsymbol{r}' \in \Gamma.$$

The integral is again a Cauchy principal-value integral whose integrand we likewise desingularize. Here, however, axisymmetry necessitates that both B_r and B_z be identically zero so that only the azimuthal contribution of the integral remains, as

$$B_\theta(s) = \int_0^\infty [\mu(s') - \mu(s)]\mathscr{K}_{\boldsymbol{B}}(s|s')\,\mathrm{d}s', \tag{2.7}$$

where

$$\begin{aligned}\mathscr{K}_{\boldsymbol{B}}(s|s') &= -\int_0^{2\pi} \boldsymbol{n}' \times \nabla_{\boldsymbol{r}'}\mathscr{G}(\boldsymbol{r}|\boldsymbol{r}')r'\,\mathrm{d}\theta' \\ &= \frac{r'}{\pi A^3}\left\{-\frac{rn_z'E(k)}{1-k} + \frac{r'n_z' + (z-z')n_r'}{k}\left[\frac{2-k}{1-k}E(k) - 2K(k)\right]\right\}.\end{aligned} \tag{2.8}$$

Finally, from the vector potential $\boldsymbol{B}$, we define a pseudo-streamfunction, ψ as

$$\psi(s) = r\boldsymbol{B}\cdot\boldsymbol{e}_\theta = rB_\theta \quad \text{with} \quad u_n = \frac{1}{r}\frac{\mathrm{d}\psi}{\mathrm{d}s}. \tag{2.9}$$

Given an initial ϕ_0, then, we first solve the Fredholm integral (2.6) for the dipole strength μ and subsequently use (2.7) to evaluate $B_\theta(s)$. Then, with knowledge of the velocities from (2.9), we use the Bernoulli equation (2.4) to evolve ϕ forward in time, while enforcing the kinematic boundary condition to evolve the surface forward in time. The process can then be repeated with the updated ϕ and the new surface profile as input. Details of the numerics are given in § 3, but before constructing them it is fruitful first to question the admissible distributions of ϕ_0 and, since the fluid domain is unbounded, deduce the asymptotic behaviour of the solution near the axis of symmetry and at large distances from it.

https://doi.org/10.1017/S0022112007004648 Published online by Cambridge University Press

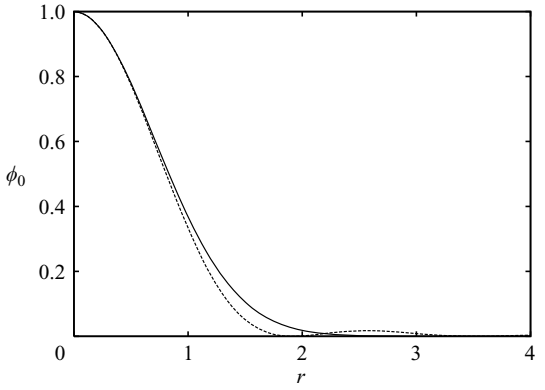


FIGURE 2. Plots $\phi_0(r, 0)$ for a Gaussian (solid line) and $[J_1(2r)/r]^2$ (dashed line).

2.4. *Admissible* ϕ_0

The interior and free surface of the physical system we are modelling is subjected to a pulse from a distant acoustic transducer whose focused nonlinearly interacting waves realize a time-averaged (over time scales $T_b \ll T$) energy-density field that is related both to the Langevin radiation-pressure field and to φ (Elrod *et al.* 1989). Kino (1987) gave the radial variation of the time-averaged energy density in the far field of such a transducer as $[J_1(2r)/r]^2$, rendering it a candidate for φ_0, where J_1 is the first-order Bessel function of the first kind. However, as we see in figure 2, $[J_1(2r)/r]^2$ is well approximated by a Gaussian, especially when $r \ll 1$, and our preference is thus to take the simple form

$$\phi_0 = \varphi|_{z=0} = \mathrm{e}^{-r^2}. \tag{2.10}$$

That being said, our choice for $\varphi(r, \theta, z)$ at $t = 0$ must be an admissible solution to (2.1) and the boundary conditions, and so it is, as we show in Appendix A. As an aside we note that $\varphi(r, \theta, z)$ may be any continuous C^2 function that vanishes as $r \to \infty$.

2.5. *Asymptotic behaviour*

Before proceeding numerically, we plan to map from the infinite to the finite domain, and we want the mapping to reflect the asymptotic behaviour of the solution. In particular, since the only independent spatial variable in the problem is the surface arclength s, we should like to know how each of the dependent variables r, z and ϕ behaves as $s \to 0$ and $s \to \infty$. Details are given in Appendix B.

In particular we find that the asymptotic forms for z and r at large s and $t = O(1)$ are given by (B 6), and the behaviour as $s \to 0$ by (B 3) and (B 4). Finally, on substituting (B 2), (B 4) and (B 6) into the evolution equation (2.4) for ϕ, the forms for $\partial\phi/\partial t$ as $s \to 0$ and $s \to \infty$ follow as:

$$\frac{\partial \phi}{\partial t} \sim \sum_{j=0}^{\infty} \bar{a}_{2j}(t) s^{2j} = \bar{a}_0(t) + \bar{a}_2(t) s^2 + \cdots \quad \text{as} \quad s \to 0, \tag{2.11}$$

$$\frac{\partial \phi}{\partial t} \sim \sum_{j=3}^{\infty} \bar{b}_j(t) j \frac{1}{s^j} = \bar{b}_3(t) \frac{1}{s^3} + \bar{b}_4(t) j \frac{1}{s^4} + \cdots \quad \text{as} \quad s \to \infty. \tag{2.12}$$

Observe that while ϕ_0 decays exponentially fast at large s its evolution decays only algebraically fast; and a similar analysis of (2.6) reveals the same disparity in the

https://doi.org/10.1017/S0022112007004648 Published online by Cambridge University Press

decay rates of μ. Thus, if we construct a mapping to recover the above algebraic response there is a conflict with our choice of ϕ_0; we address this now in § 2.6.

2.6. *Decomposition*

To resolve the conflict just mentioned we decompose the velocity potential into $\phi_0+\phi$ and now identify ϕ as the growth from ϕ_0 as the system evolves. The numerics then need to describe only features of ϕ which necessarily will decay as in (2.12), while ϕ_0 can be any arbitrary analytic input function that satisfies (2.1). In effect the decomposition renders the numerical algorithm independent of the chosen ϕ_0. In a similar manner we decompose the dipole strength into $\mu_0+\mu$ and identify μ as the growth in μ from its initial value μ_0. Then (2.4) is unchanged and, since μ_0 is specified in advance, (2.6) becomes a Fredholm integral equation for the increase in dipole strength μ:

$$\phi(s)=\frac{1}{2}\mu(s)+\int_0^\infty [(\mu_0(s')+\mu(s'))-(\mu_0(s)+\mu(s))]\,K_\phi(s,s')\,\mathrm{d}s'. \tag{2.13}$$

A further benefit of this decomposition is that the derivatives of ϕ_0 and μ_0 are always known analytically and, since they contain the bulk of the energy (at least initially), the error in evaluating sensitive terms similar to the surface derivative of the velocity potential $\mathrm{d}(\phi_0+\phi)/\mathrm{d}s$ is minimal, because $\mathrm{d}\phi_0/\mathrm{d}s$ is known exactly and $|\mathrm{d}\phi_0/\mathrm{d}s|\gg|\mathrm{d}\phi/\mathrm{d}s|$ for small t.

3. Numerics

To proceed numerically, we first introduce a mapping from the semi-infinite line s to the finite line η. We then express each of the dependent variables $\{r, z, \phi, \psi, \mu\}$ in terms of basis functions over η. Unknown, of course, are the coefficients of the basis functions and, for reasons discussed below, we use a collocation method to deduce those for $\{r, z, \phi, \psi\}$ and a Galerkin method for those relating to μ.

In order to follow the evolution of the (initially flat, $z=0$) surface we place on it Lagrangian markers, each located by its radial coordinate $r(s)$ and vertical coordinate $z(s)$, and monitor them. The markers, together with the velocity potential $\phi(s)$, form the triple $\{r, z, \phi\}$ that defines the primary dependent variables of the system, and these are supplemented by the further dependent variables ψ and μ. The numerical solution involves marching these variables forward in time.

For example, given the normal and tangential velocities $\boldsymbol{u}=(u_n, u_t)$ at the surface, the location coordinates of the markers, r and z, are evolved kinematically as

$$\frac{\mathrm{d}r}{\mathrm{d}t}=u_t n_z+u_n n_r \quad \text{and} \quad \frac{\mathrm{d}z}{\mathrm{d}t}=u_n n_z-u_t n_r, \tag{3.1}$$

where u_n is given by (2.9) and u_t by (3.11) below. The evolution of ϕ is via the Bernoulli equation (2.4) with the partial derivative written as a material derivative, i.e. $\mathrm{D}/\mathrm{D}t=\partial/\partial t+\boldsymbol{u}\cdot\nabla$, so that

$$\frac{\mathrm{d}\phi}{\mathrm{d}t}=\frac{1}{2}u_n^2+\frac{\mathrm{d}\phi}{\mathrm{d}s}\left(\frac{1}{2}u_t-\frac{\mathrm{d}\phi}{\mathrm{d}s}\right)-\frac{1}{We}\kappa-\frac{1}{Fr}z. \tag{3.2}$$

Updated values of $\{r, z, \phi\}$ are then used to calculate the dipole strength by solving the Fredholm integral (2.13), after which the process is repeated.

In doing so, of course, the evolution equations (3.1) and (3.2) for r, z and ϕ require computation of surface derivatives through terms such as $n_z\equiv\mathrm{d}r/\mathrm{d}s$, $n_r\equiv-\mathrm{d}z/\mathrm{d}s$

https://doi.org/10.1017/S0022112007004648 Published online by Cambridge University Press

and κ. Of these the curvatures, κ requires derivatives of the highest order, viz

$$\kappa = \kappa_r + \kappa_\theta \quad \text{where} \quad \kappa_r = \frac{\mathrm{d}r}{\mathrm{d}s}\frac{\mathrm{d}^2z}{\mathrm{d}s^2} - \frac{\mathrm{d}z}{\mathrm{d}s}\frac{\mathrm{d}^2r}{\mathrm{d}s^2} \quad \text{and} \quad \kappa_\theta = \frac{1}{r}\frac{\mathrm{d}z}{\mathrm{d}s} \tag{3.3}$$

Here κ_r and κ_θ refer to the radial and azimuthal curvature respectively.

3.1. *Mapping*

Numerically it is best not to employ the primary independent variable s on an unbounded domain. We have two choices: arbitrarily to truncate the domain at large but finite s, or to use a mapping to transform the physical domain into a finite computational domain. The latter is optimal, but we must be prudent in our choice of mapping. Specifically, to concur with our analytical solutions we should choose a mapping that depicts algebraic decay, which means that we must exclude candidate mappings such as $\eta = 2\tanh s - 1$. In fact it is expedient to tailor-make our own mapping, as then we can precisely control the asymptotic behaviour of the solutions to match the known analytic solutions given in § 2.5.

In constructing such a mapping, we must require, from (B 2), (B 4) and (B 6), that it contains all positive even powers of s as $s \to 0$ and both odd and even negative powers of s as $s \to \infty$. The former requirement is readily satisfied with a term of the form $(1 + s^2)^{-1}$, but this introduces only negative even powers of s for large s. In order also to introduce negative odd powers of s for large s (without introducing positive odd powers as $s \to 0$) we include a second term $(1 + s^2)^{-1/2}$ and adjust the relative strength of each term through a parameter $\alpha \in [0, 1]$. For generality we can also scale s, by replacing it by βs and adjusting the value of β, but this was not found to be necessary. Finally, in anticipation of employing Chebyshev polynomials as basis functions, we introduce the transformed independent variable $\eta(s)$ in the transformed domain $[-1, +1)$ and obtain the invertible mapping

$$\eta(s) = 1 - 2\left(\frac{\alpha}{s^2+1} + \frac{1-\alpha}{\sqrt{s^2+1}}\right). \tag{3.4}$$

Various values of α were tested but $\alpha = 1/2$ worked well and was used in all the simulations performed.

3.2. *Interpolation and numerical derivatives of the surface*

Interpolation is necessary when the quadrature points used to evaluate the Fredhom integral (2.13) (and the pseudo-streamfunction (2.7)) do not coincide with the collocation points. We must also reliably compute surface derivatives to evaluate κ, (3.3).

In order to both interpolate and evaluate the derivatives, therefore, we expand each dependent variable $\chi = \{r, z, \phi, \psi, \mu\}$ as a series of Chebyshev polynomials $T_i(\eta)$, viz.

$$\chi(s) = f_\chi(s)\sum_{i=0}^{N} C_i^\chi T_i(\eta(s)) \quad \text{where} \quad \chi = \{z, r, \phi, \psi, \mu\}, \tag{3.5}$$

rendering our problem as one of finding the unknown coefficients C_i^χ. Boundary conditions, such as $\mathrm{d}r/\mathrm{d}s|_{s=0} = 1$ and $\mathrm{d}z/\mathrm{d}s|_{s=0} = 0$ are implemented by the multiplication of a predetermined function f_χ, chosen to ensure the correct asymptotic behaviour as $s \to 0$ and $s \to \infty$. For example, the function chosen for z, ϕ and μ is $f_z(s) = f_\phi(s) = f_\mu(s) = (1 + s^2)^{-3/2} = \mathfrak{f}(s)$, say.

We note, however, that since the expansions for r and z are determined independently, the arclength metric will not in general be identically unity. Thus

https://doi.org/10.1017/S0022112007004648 Published online by Cambridge University Press

either we enforce unity by expressing r or z through the respective integrals

$$r = \pm \int_0^s \mathrm{d}s' \sqrt{1 - \left(\frac{\mathrm{d}z}{\mathrm{d}s'}\right)^2} \quad \text{or} \quad z = \pm \int_0^s \mathrm{d}s' \sqrt{1 - \left(\frac{\mathrm{d}r}{\mathrm{d}s'}\right)^2},$$

or we ensure unity by normalizing the derivatives by the computed arclength metric, which is equivalent to saying that rather than being the true arclength, s is a Lagrangian variable that approximates (albeit closely) the arclength. The former is more computationally intensive, because it involves numerical quadrature and keeping track of when the surface 'folds over', in order to choose the correct sign for the integrand. For that reason we opt to normalize.

Lastly, with the exception of C_i^μ, discussed below in § 3.3, the coefficients of each Chebyshev polynomial C_i^χ were determined through collocation using the FFT algorithm given by Fornberg (1996). The basis-function number $N = 64$ was found to provide an adequate balance between resolution and computational effort for most of the computations performed.

3.3. *Solution of Fredholm integral*

It remains to determine the unknown coefficients C_i^μ. To do this we note that the Fredholm integral (2.6) for μ is linear in μ, which means that we may take a Galerkin projection of (2.6) to obtain a linear system for the C_i^μ.

So, after substituting the expansions for ϕ and μ given in (3.5) into (2.13), we get

$$f_\phi(s) \sum_{i=1}^{N} C_i^\phi T_i(\eta(s)) = \tfrac{1}{2} f_\mu(s) \sum_{i=1}^{N} C_i^\mu T_i(\eta(s)) + \int_0^\infty \Delta\mu(s, s') \mathscr{K}_\phi(s|s')\, \mathrm{d}s' + R(s), \quad (3.6)$$

where

$$\Delta\mu(s, s') = \mu_0(s') - \mu_0(s) + \sum_{i=0}^{N} \Delta\mu^i(s, s')$$

and

$$\Delta\mu^i(s, s') = f_\mu(s') C_i^\mu T_i(\eta(s')) - f_\mu(s) C_i^\mu T_i(\eta(s)).$$

Then, to determine the unknown coefficients, we demand that the residual $R(s)$ normalized by $\mathfrak{f}(s)$ be orthogonal with respect to the N basis functions, i.e. the Chebyshev polynomials $T_i(\eta)$ (for details see Phillips & Wu 1994). We then find that

$$C_j^\phi = \left(\tfrac{1}{2}\delta_{ij} + M_{ij}\right) C_i^\mu + A_i, \quad (3.7)$$

where δ_{ij} is the Kronecker delta and

$$M_{ij} = \int_{-1}^{+1} \frac{1}{\mathfrak{f}[s(\eta)]} \left\{ \int_0^\infty \Delta\mu^i(s, s') \mathscr{K}_\phi(s|s')\, \mathrm{d}s' \right\} \frac{T_j(\eta(s))}{\sqrt{1-\eta^2}}\, \mathrm{d}\eta \quad (3.8)$$

with

$$A_j = \int_{-1}^{+1} \frac{1}{\mathfrak{f}[s(\eta)]} \left\{ \int_0^\infty [\mu_0(s') - \mu_0(s)] \mathscr{K}_\phi(s|s')\, \mathrm{d}s' \right\} \frac{T_j(\eta(s))}{\sqrt{1-\eta^2}}\, \mathrm{d}\eta. \quad (3.9)$$

Equation (3.7) is a linear algebraic system where M_{ij} is fully populated, so an LU decomposition is used to solve the system for C_i^μ. Prior to solving (3.7), however, we must evaluate the integrals within M_{ij} and A_j; we use Gauss–Kronrod quadrature for the inner integral (shown in curly brackets; see also § 3.4 below) and an FFT for the outer integral.

https://doi.org/10.1017/S0022112007004648 Published online by Cambridge University Press

3.4. *Numerical quadrature*

The inner integrals in (3.8) and (3.9) were evaluated using Gauss–Kronrod quadrature. The strength of the Gauss–Kronrod quadrature over Gauss–Legendre lies in its adaptive capabilities, in that we can prescribe a required accuracy and then quadrature points are added iteratively until the desired accuracy is achieved. It is also efficient computationally, as evaluations of the integrands in the previous iteration are reused with adjusted weights. Nie & Baker (1998) employed the same technique in their vortex-sheet calculations. For the computations herein we typically set the relative accuracy ϵ to 10^{-12}.

We must also pay attention to the weak singularity in the integrand of (3.8). This singularity occurs because the derivative of the integrand becomes discontinuous as the integration point s' approaches the source point s, even though the integrand itself is continuous. For example, on expanding the integrand in (3.8) about s we observe the asymptotic behaviour

$$[\mu(s') - \mu(s)]\mathscr{K}_\phi \sim (s - s')\log|s - s'|, \tag{3.10}$$

which suggests that in the interval $[s - \delta s, s + \delta s]$, the integral is $O(\delta s^2 \log|\delta s|)$. In consequence we evaluate the integral in two parts, the first in the interval $[0, s - \delta s]$ and the second in the interval $[s + \delta s, \infty)$, with δs chosen to ensure that the relative accuracy ϵ prescribed for the Gauss–Kronrod quadrature is preserved. In this way, we avoid evaluating the integrand at or near the singularity. The same strategy is adopted for evaluating ψ in (2.7).

3.5. *Choice u_t*

Because tangential deformations do not affect the shape of the surface, u_t may be chosen in any convenient way. The usual choice, $u_t = d\phi/ds$, is commonly termed the Lagrangian frame, because each marker evolves with its physical velocity. The disadvantage of the Lagrangian frame, however, is that it leads to clustering of the marker points at some locations on the surface, which in turns leads to numerical-stability issues for long-time evolution. Since the time step Δt required for stability scales with the minimum distance between successive markers, an ever-decreasing Δt is required as the surface evolves, making the Lagrangian frame computationally inefficient. Furthermore, clustering has the result that some regions are under-resolved and others are over-resolved. So, in order to maintain an acceptable level of resolution, either more points have to be inserted or the points have to be remeshed or redistributed, which again increases the computational cost, not to mention the errors due to repeated remeshing and redistribution.

A way to circumvent these problems is to impose a choice of u_t that renders the distance between successive marker points constant in time. This idea was proposed by Hou *et al.* (1994) and has been successfully used by them and others to solve two-dimensional and axisymmetric free-surface problems involving surface tension in both finite and periodic domains (Hou *et al.* 1997, 2001; Nie 2001). We will follow suit; u_t is then determined through the curvature and the normal velocity u_n as

$$u_t(s) = \int_0^s u_n(s')\kappa_r(s')\,\mathrm{d}s'. \tag{3.11}$$

Finally we point out that this choice (for u_t) is especially useful in a Chebyshev collocation implementation because s, and thus η, for each collocation point is then fixed in time. Thus the values at the collocation point can be used directly, without interpolation back to the Chebyshev point.

https://doi.org/10.1017/S0022112007004648 Published online by Cambridge University Press

3.6. *Time integration and filtering*

An explicit fourth-order Runge–Kutta scheme was used for time integration. This was chosen over a full or semi-implicit scheme because of the nonlinearity of the evolution equations and, more importantly, the need to solve a Fredholm integral equation as an intermediate step. For the same reasons, collocation was chosen over Galerkin projection in the evaluation of the nonlinear evolution equations (2.7), (3.1) and (3.2) to simplify the numerical implementation. The disadvantage of this choice is that aliasing errors are introduced, which, if left uncontrolled, quickly amplify and dominate the calculation. A Fourier-type filter of the form (Hou *et al.* 1994)

$$C^{\chi}_{j_{\text{filtered}}} = \mathrm{e}^{-\gamma(j/N)^m} C^{\chi}_{j} \quad \text{for} \quad \chi = \{z, r, \phi, \psi\} \tag{3.12}$$

was thus used to remove the high-wavenumber instability induced by aliasing errors. Filtering was used to remove all wave components whose amplitude fell below a certain threshold value ε. Typical values used for the computations were $\gamma = 10$, $m = 10$ and $\varepsilon = 10^{-12}$. The filters were applied before the start of each Runge–Kutta step.

4. Results

Given an impulse $\phi_0(r)$, which in dimensional form is a measure of the incident acoustic pressure and period (see § 5.3 below), the initially flat free surface evolves subject to two parameters, the Froude number, which is a measure (inverse) of the role of gravity, and the Weber number, which reflects (inversely) the role of surface tension through the local surface curvature. In discussing our results, therefore, we first investigate (in § 4.1) the double limit in which neither gravity nor surface tension play a role, viz. $We^{-1} \to 0$, $Fr^{-1} \to 0$. We then remove one driving force while we investigate the other (§§ 4.2, 4.3). Finally, in § 4.4, we allow both gravity and surface tension to play a role.

4.1. *The double limit: $We^{-1} \to 0$, $Fr^{-1} \to 0$*

Our problem is analogous to the evolution of an initially flat vortex sheet whose strength is proportional to $\phi_0(r)$. Vortex sheets are susceptible to a Kelvin–Helmholtz instability; indeed, the smaller the wavelength of the instability the faster the growth rate. Mathematically this may suggest that the initial-value problem for the evolution of the interface is ill-posed (Moore 1979). Computationally, the absence of any mechanism to damp the high-wavenumber modes means they quickly amplify and dominate the calculation (Moore 1976).

Since we are not modelling the air above the free surface it is inappropriate to label any instability we encounter as a Kelvin–Helmholtz instability. Nevertheless we expect to find the manifestation of a like instability in the double limit $We^{-1} \to 0$ and $Fr^{-1} \to 0$ and, of course, we do so, as we see in figure 3(*a*). Here the dashed curve in the inset indicates the presence of the high-frequency modes, which, in this instance, prevented the simulation from being carried out reliably for $t > 0.66$. This cutoff was not affected by doubling or halving the time step in the calculation but was affected by altering the number of surface marker points. Thus, since the latter is tantamount to a high-wavenumber cutoff in the calculation, our inference is that the instability is numerical.

Of course, in the absence of any restoring mechanism, and since self-induction is symmetrical about $r = 0$, we expect the axisymmetric surface jet to reflect the initial condition (B 1) always and not to form a droplet, and this is the case, at least for

https://doi.org/10.1017/S0022112007004648 Published online by Cambridge University Press

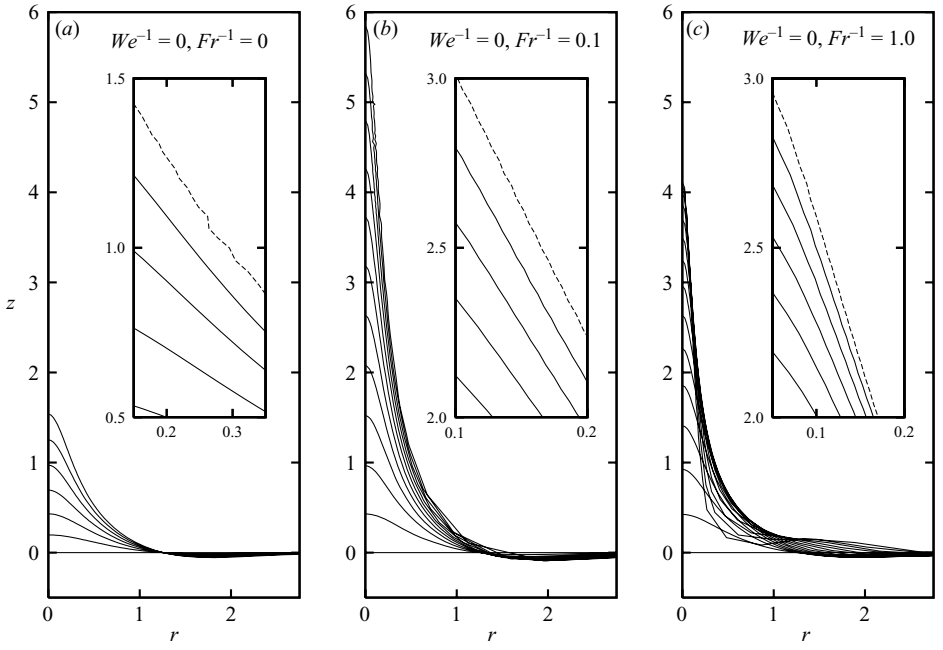


FIGURE 3. The surface profile, z vs. r, for various Froude numbers such that $1/Fr^2 = 0, 0.1, 1$, with $We^{-1} = 0$. We use the following notation: start time [time increment between profiles] terminal time. Then we have (*a*) $t = 0$ [0.1] 0.66, (*b*) $t = 0$ [0.2] 2.28 and (*c*) $t = 0$ [0.2] 2.90. The inserts shows the profiles at time steps immediately prior (solid lines) to the onset of a numerical instability (dashed line).

the duration of the calculation. Moreover, were the calculation to proceed for times $t > 0.66$, there would be no limit on the amplitude and for that reason we would refer to it as a jet.

4.2. *Infinite Weber number* ($We^{-1} \to 0$) *and finite froude number*

Gravity acts to bound the amplitude of the axisymmetric surface jet, rendering it a wave. It is unclear whether gravity is able to suppress the instability. To gain insight into this question we repeated the simulation at finite Froude number, specifically at $Fr^{-1} = 0.1$ and $Fr^{-1} = 1$. The results are presented in figures 3(*b*) and 3(*c*). We found (see the insets) that instability overwhelms the calculation before gravity limits the amplitude of the wave. Nevertheless gravity does act to retard the onset of instability, thereby allowing the system to evolve over longer times, namely $t \approx 2.28$ and $t \approx 2.90$ as compared with $t \approx 0.66$ in § 4.1.

To understand the longer evolution, we note that whereas damping due to gravity is local and proportional to the local elevation z, the instability is not restricted to wavenumbers of $O(z^{-1})$ and may arise everywhere (i.e. at all r). In other words, although gravity acts to damp unstable modes of wavenumber greater than $O(z^{-1})$ locally (i.e. at particular r values), it has a diminishing effect on modes of wavenumber less than $O(z^{-1})$. This suggests that gravity-induced damping will never be sufficient to self-regulate all modes. In contrast, the damping due to surface tension is proportional to the curvature. So, since the high-wavenumber mode induces high curvature, there is a self-checking mechanism in place to inhibit the growth of such modes, as we shall see in the following section.

https://doi.org/10.1017/S0022112007004648 Published online by Cambridge University Press

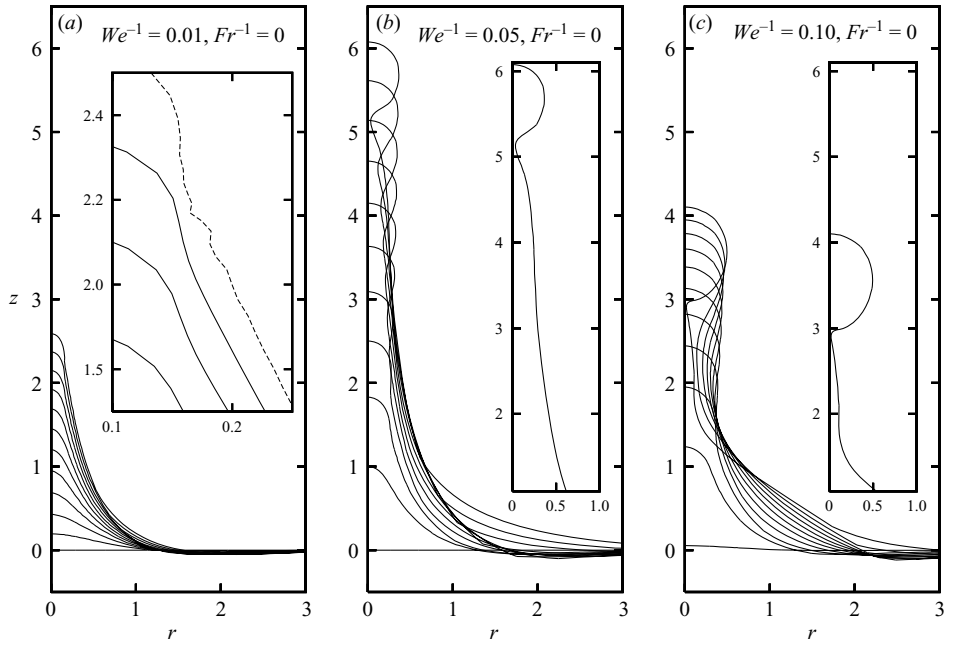


FIGURE 4. Surface profiles of z vs. r at various inverse Weber numbers We^{-1}. The time interval between successive snapshots is 0.1, 0.45 and 0.6 in (a), (b) and (c) respectively. In (a) the Weber number is such that $We^{-1} < We_c^{-1}$. Here instability occurs even in the presence of surface tension. This is evident in the insert, which shows profiles at time steps (solid lines) leading up to the onset of the instability (dashed line). The insets in (b) and (c) show the surface profile just before the drop is formed; panel (c) is the case studied by Elrod *et al.* (1989).

4.3. *Finite Weber number in zero gravity* ($Fr^{-1} \to 0$)

The effects of surface tension are twofold: first, it acts to render the problem well-posed and second, it acts to regularize the instability (Pullin 1982). That said, we should not expect all $We^{-1} > 0$ to suppress the instability; rather, suppression is likely only above some critical threshold, We_c^{-1} say, beyond which the computation can be carried out reliably over times long with respect to T. Our first task then is to determine We_c^{-1}. We should then like to know how surface tension affects the diameter of the droplets and the velocity at which they are ejected. So, to this end, we performed computations over a range of Weber numbers from $We^{-1} = 0$ to $We^{-1} = 0.15$ and, to exclude the role of gravity, we set $Fr^{-1} = 0$. The time evolution for three different Weber numbers is shown in figure 4.

A typical result for $We^{-1} \ll We_c^{-1}$ is presented in figure 4(a). Here, as seen in the inset, high-frequency contributions indicative of the instability lead to a non-smooth surface profile immediately prior to termination of the simulation. The instability dominates until $We_c^{-1} \approx 0.045$, above which we are able to follow the evolution of the surface to near-pinchoff. But we cannot predict beyond pinchoff because the continuum hypothesis (and thus our formulation) then breaks down. Pinchoff is the point at which the radial coordinate of the surface vanishes at a position $s > 0$. We see this in figures 4(b) and 4(c), where of course $We^{-1} > We_c^{-1}$. Observe too that the size of the drop-to-be increases as We^{-1} increases. However, since a higher We^{-1}

https://doi.org/10.1017/S0022112007004648 Published online by Cambridge University Press

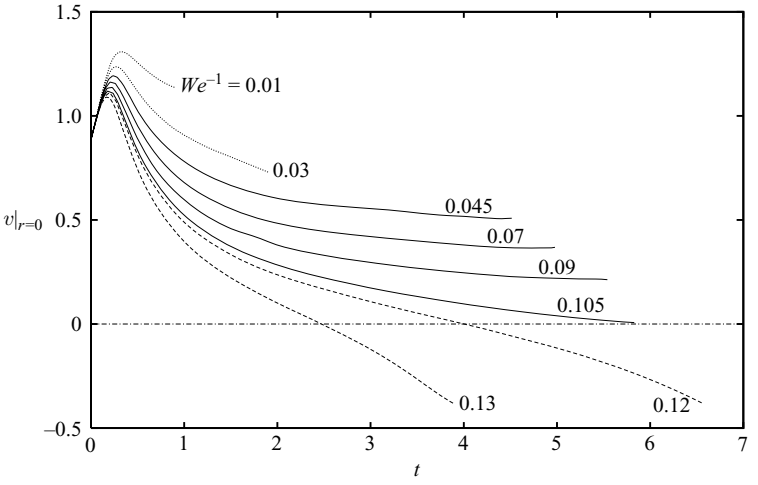


FIGURE 5. Plots of centreline velocity $v|_{r=0}$ against time for $Fr^{-1} = 0$ and various inverse Weber numbers We^{-1}. The dotted lines indicate cases where the simulation terminated due to instability. The solid lines indicate cases where droplets were formed: the lines terminate at the time at which this happened; see also figure 6(*a*). The dashed lines indicate cases where drops did not form owing to the level of surface tension.

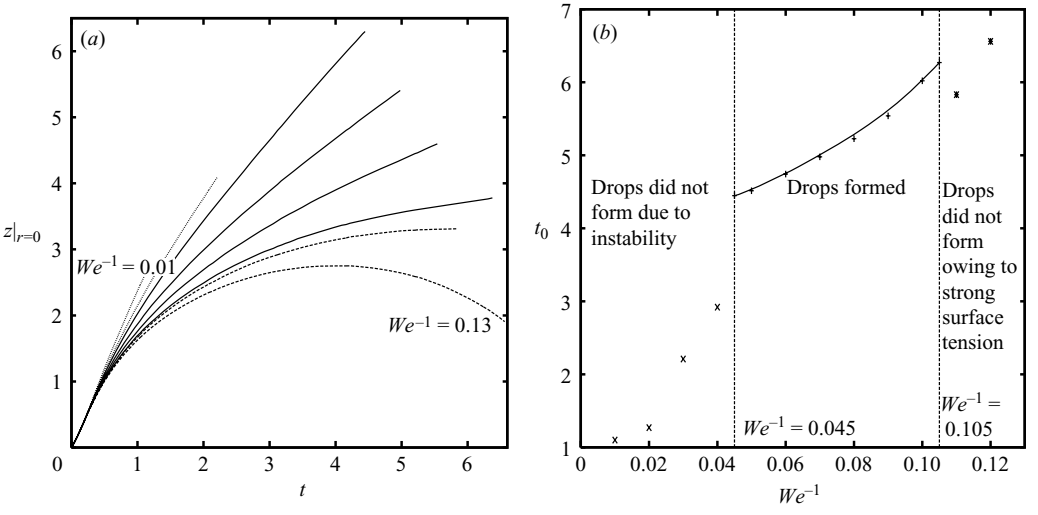


FIGURE 6. Plots of (*a*) centreline elevation $z|_{r=0}$ against time for $Fr^{-1} = 0$ and various inverse Weber numbers We^{-1}. The dotted lines (lying above the solid lines) indicate cases where the simulation terminated due to instability. The solid lines indicate cases where droplets were formed. The dashed lines indicate cases where drops did not form owing to the level of surface tension. The lines terminate at the time t_0 at which the drop formed or the calculation terminated. In (*b*) the terminal time t_0 is shown against We^{-1}.

implies stronger surface tension and thus a higher resistance to the flow, the height and velocity at which the droplet is ejected is reduced.

Figure 5 details the variation in the centreline velocity and figure 6(*a*) gives the centreline elevation as a function of time. Cases that failed due to numerical instabilities prior to the formation of the drops, i.e. for $We^{-1} < We_c^{-1}$, are indicated

https://doi.org/10.1017/S0022112007004648 Published online by Cambridge University Press

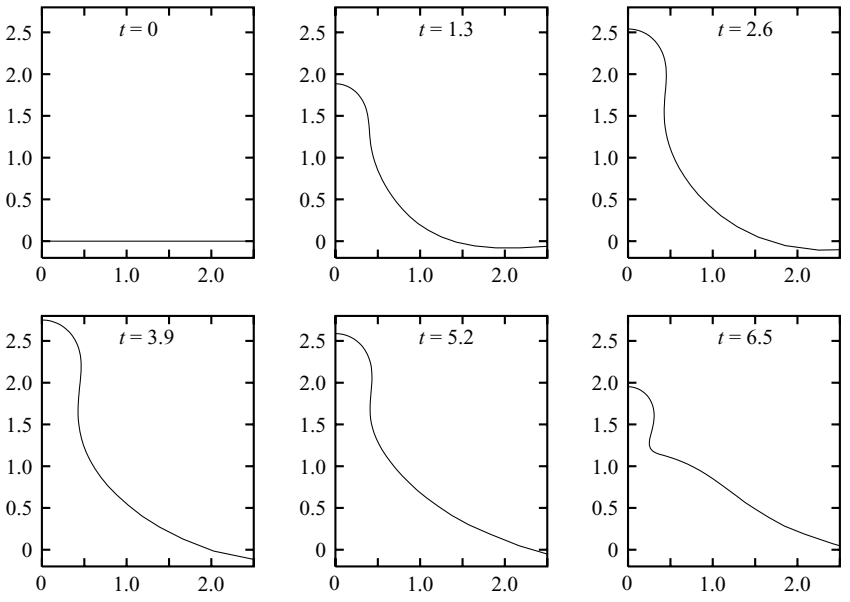


FIGURE 7. Time evolution of the surface profile when $We^{-1} = 0.12$ and $Fr^{-1} = 0$. Here a droplet was not formed; rather a peak amplitude was attained at about $t = 3.9$ and the fluid then collapsed on itself under the restoring effect of surface tension, resulting for $t \gg 6.5$ in a standing wave.

with dotted lines, while the solid lines indicate Weber numbers where we were able to carry the simulation near to the formation of a drop, viz. for $We^{-1} > We_c^{-1}$. Of course whether We_c^{-1} is the actual physical demarcation at which single drops form or an inflated value more representative of the value of We^{-1} at which numerical instabilities are brought under control is inconclusive.

Nevertheless, we do have an upper bound, We_0^{-1}. Specifically, since a higher inverse Weber number reflects a greater resistance to the flow, there comes a point at which the initial energy imparted to the system through ϕ_0 is insufficient to overcome the restraints of surface tension. This limiting case is evident in figure 5 as the curve where the centerline velocity asymptotes to zero just as the droplet is formed, suggesting that $We_0^{-1} \approx 0.105$.

Cases for $We^{-1} > We_0^{-1}$ in figure 5 are indicated with dashed lines. Thus, in addition to a region for $We^{-1} < We_c^{-1}$ dominated by the instability and a second for $We^{-1} \in [We_c^{-1}, We_0^{-1}]$ in which single droplets form, the case $We^{-1} > We_0^{-1}$ highlights a third region. Herein the centreline velocity changes from positive to negative in accord with the free surface, which reaches a maximum height and then subsides, as evident in figure 6(*a*). Indeed, beyond We_0^{-1} the fluid is no longer capable of ejecting a droplet. Rather, the third region highlights the formation of an axisymmetric standing wave which grows and then subsides. The time evolution as a series of free-surface 'snapshots' of one such case at $We^{-1} = 0.12$ is presented in figure 7.

The curves in figures 5 and 6(*a*) finish at t_0, the time at which the calculation terminated because of an instability, surface tension or the formation of a droplet. These times are plotted in figure 6(*b*). Finally, we emphasize that these simulations are performed with gravity set to zero, so that the restoring force is entirely due to surface tension; we shall allow for non-zero gravity in § 4.4.

https://doi.org/10.1017/S0022112007004648 Published online by Cambridge University Press

4.4. *Finite Weber number and Finite Froude number*

We turn our attention now to cases where both We^{-1} and Fr^{-1} are non-zero. In doing so we fixed the inverse Weber number We^{-1} as 0.08, which is within the range of Weber numbers where droplets form under zero gravity, and repeated the simulation over more than an order of magnitude of Froude numbers, including negative values. The results are presented in figure 8.

Observe that except for the height at which the droplets are formed, which is clearly a gravitational effect, there are no major differences in the generic formation of the drops for $Fr^{-1} \in [-0.1, 0.1]$. Indeed, as we see in figures 8(*a–c*), the size of the droplets is roughly the same even when we reverse the direction of gravity (relative to z). Eventually, however, gravity overrides the impulse and the standing axisymmetric wave so formed rises and then collapses upon itself, much as we would expect a standing gravity wave to behave. Inverted tear-shaped droplets can then form during the collapse process, as we see in figures 8(*d*) and 8(*e*). Observe, however, that while 8(*d*) depicts a double-point pinchoff during collapse, 8(*e*) highlights a single-point collapse. Further increases in Fr^{-1} depict only a collapsing wave. Finally, unlike the surface-tension-dominated collapse in figure 7, which rapidly damps the wave with minimal oscillation, gravity damping under weak surface tension is much slower, with noticeable oscillation, as shown in figure 8(*f*).

4.5. *Phase diagram*

Our results are summarized in figure 9, in which we plot Fr^{-1} versus We^{-1}. For example, with $Fr^{-1} = 0.125$ we observe, with increasing We^{-1} above the instability cutoff $We^{-1} \approx 0.045$, first the formation of spherical drops-then inverse tear-shaped drops and finally axisymmetric standing waves. Spherical drops no longer form if $Fr^{-1} = 0.5$, however; rather, inverted tear-shaped drops followed by axisymmetric waves. Lastly, no drops form if $Fr^{-1} = 1$, only axisymmetric waves. Not included in figure 9, of course, is the point representing the double limit $Fr^{-1} \to 0$, $We^{-1} \to 0$ at which axisymmetric jets form.

5. Discussion

5.1. *Finite-time singularity*

The problem under study here is an example where a singularity is formed in finite time, the bifurcation being a topological singularity where the surface self-intersects at time $t = t_0$. Of particular interest is how the system approaches this singularity. This was first addressed in the context of a pendant drop evolving from the end of a nozzle, an event that Peregrine, Shoker & Symon (1990) captured in a very clear sequence of photographs. These photographs show that the liquid region consists of an almost spherical drop connected (immediately prior to the bifurcation) through a liquid bridge to a conically shaped region not dissimilar to that in figures 8(*a–c*). Eggers (1993) modelled the phenomenon using a long–wave approximation of the Navier–Stokes equations, which Eggers & Dupont (1994) used finite-difference techniques to solve. Their results compare well with the photographs. In contrast Schulkes (1994) questioned how the pendant drop evolves when the volume of the drop increases steadily with time. He makes no long-wave approximation and proceeds instead using a boundary-integral formulation assuming, as we do, an inviscid irrotational flow. His results compare very well with the photographs of Peregrine *et al.* (1990).

Mathematically, the self-intersection of the surface may be precisely expressed as $r(s \neq 0) = 0$, where the radial coordinate vanishes for some location $s \neq 0$. To proceed,

https://doi.org/10.1017/S0022112007004648 Published online by Cambridge University Press

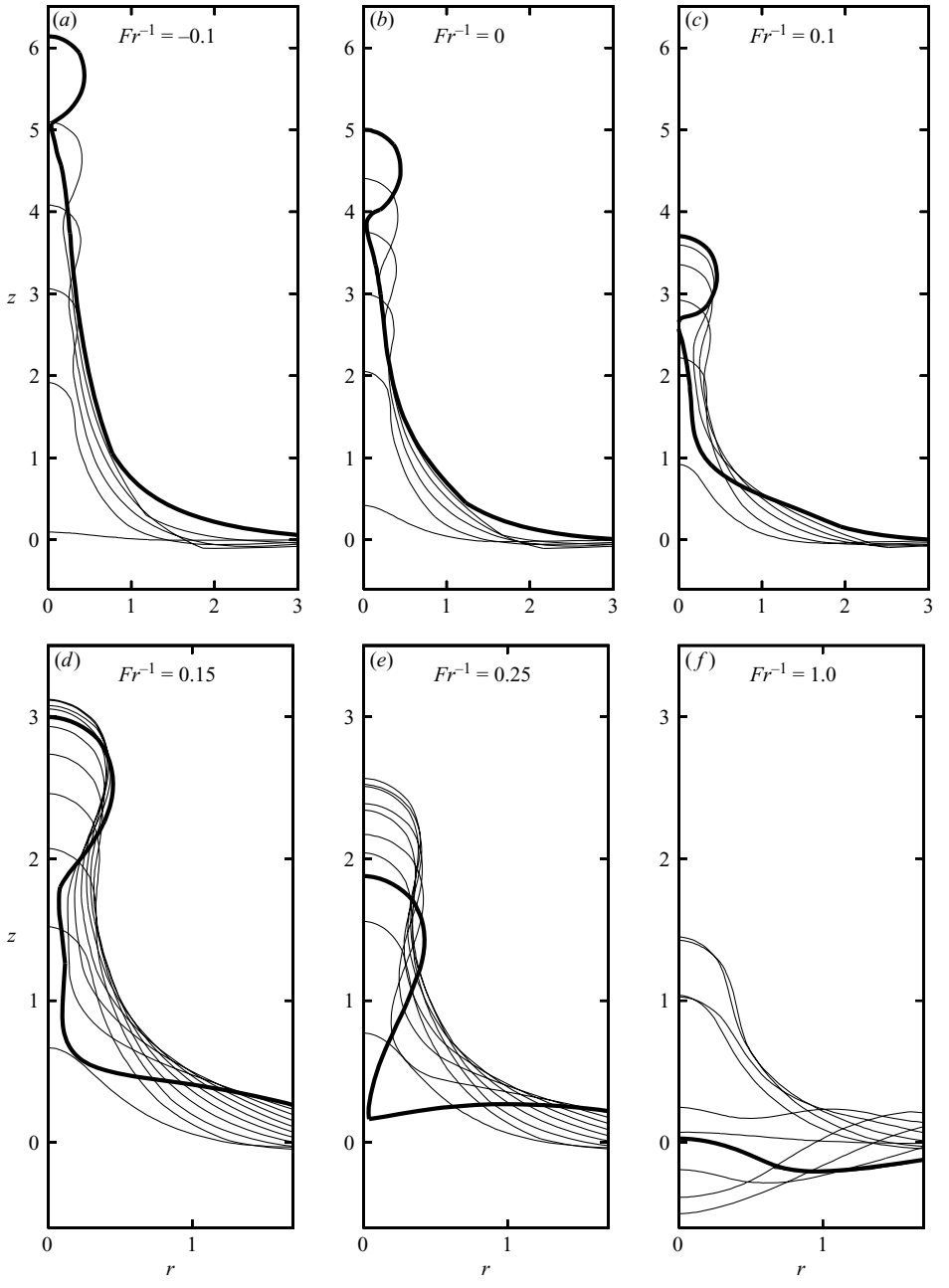


FIGURE 8. Surface profiles of z vs. r for $We^{-1} = 0.08$ and inverse Froude numbers Fr^{-1} from -0.1 to 1. Successive 'snapshots' are relative to the terminal times t_0, which were, for cases (a)–(f) respectively, $t_0 = 5.05$, 5.20, 5.43, 5.31, 4.86 and 4.54. The time interval between successive snapshots is 1.0 in cases (a)–(c) and 0.5 in cases (d)–(f). For $Fr^{-1} \leqslant 0.1$ an essentially spherical drop is formed. At larger levels of gravity we observed (inverted) tear-shaped drops that form as the wave collapses upon itself. In particular (d) shows a double pinchoff while (e) shows a single pinchoff. No drop occurs in (f), where the wave collapses and then decays.

https://doi.org/10.1017/S0022112007004648 Published online by Cambridge University Press

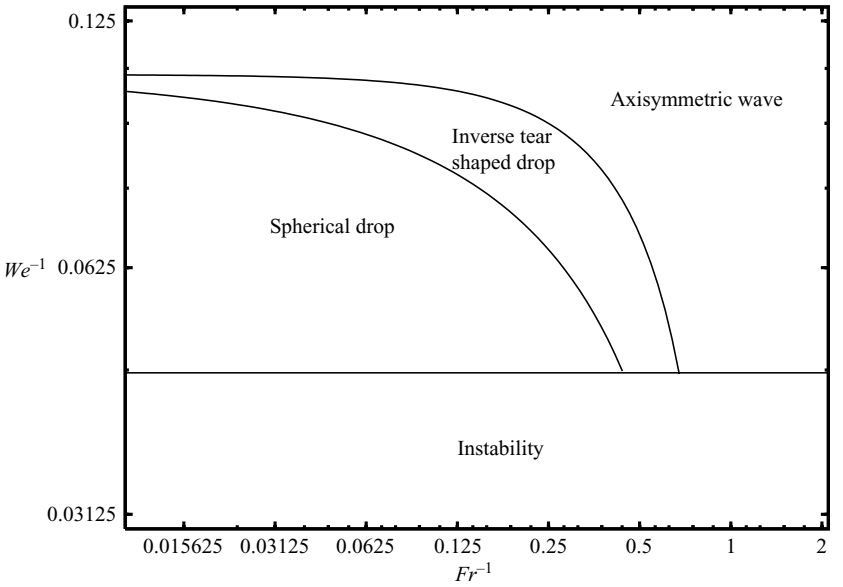


FIGURE 9. Phase diagram of Fr^{-1} vs. We^{-1} showing the regions of instability, spherical drops, inverse tear-shaped drops and axisymmetric standing waves. Not shown is the double limit $Fr^{-1} \to 0$, $We^{-1} \to 0$ at which axisymmetric jets form.

therefore, we define a radius, r_{min} say, and track it as the surface evolves. Thus let r_{min} be the radial coordinate of the point on the surface satisfying the following two conditions:

$$\frac{\mathrm{d}r}{\mathrm{d}s} = 0 \quad \text{and} \quad \frac{\mathrm{d}^2 r}{\mathrm{d}s^2} > 0, \tag{5.1}$$

which decree that there will be a solution for r_{min} only after the surface becomes vertical at some location.

The variation in r_{min} with time is given in figure 10(a). Here the 'like-shapes' of various cases suggest the existence of a self-similar solution and, because of the infinite slope of the curves at $t = t_0$, that the solution exhibits a power-law-type singularity of the form $(t_0 - t)^{\gamma}$, where the exponent $\gamma < 1$. To investigate this further we ploted $\log |r_{min}|$ against $\log |t_0 - t|$ and found that $\gamma \approx 2/3$.

Power-law behaviour can also be argued on dimensional grounds, as Keller & Miksis (1983) did, albeit in the context of a two-dimensional geometry *after* pinchoff, rather than a three-dimensional axisymmetric geometry prior to pinchoff. We start from the assumption that the behaviour should, near the singularity time, be independent of the initial conditions and thus that the relevant (dimensional) parameters are σ, ρ, r^*_{min} and $t^*_0 - t^*$. From this set of parameters, the Buckingham pi theorem indicates that we can form only one dimensionless group, which must itself be a universal constant, $\mathfrak{K}$ say. Then

$$\frac{\rho {r^*}^3_{\min}}{\sigma (t^*_0 - t^*)^2} = \mathfrak{K}^3,$$

from which we obtain a scaling relationship in terms of the Weber number:

$$r_{min} = \mathfrak{K}(t_0 - t)^{2/3}\ We^{-1/3}, \tag{5.2}$$

https://doi.org/10.1017/S0022112007004648 Published online by Cambridge University Press

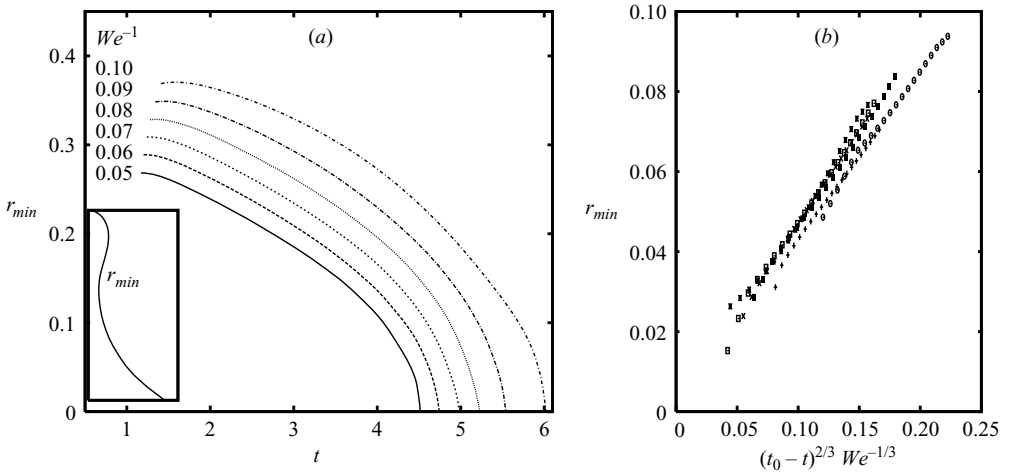


FIGURE 10. Plots of r_{min} (*a*) against time for various inverse Weber numbers We^{-1} and (*b*) in a collapsed form from (5.2), depicting the exponent $\gamma = 2/3$. The symbols are as in figure 9.

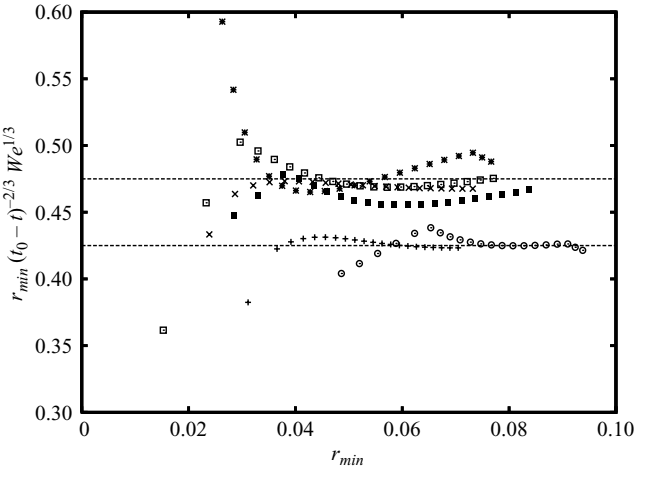


FIGURE 11. Plot of the universal constant $\mathfrak{K}^{-1}$ from (5.2) against r_{min} for various inverse Weber numbers We^{-1} for which drops form. In each instance the largest r_{min} indicates the point at which (5.1) is first satisfied. The symbols [+, ×, ∗, □, ■, ⊙] indicate respectively $We^{-1} = [0.05, 0.06, 0.07, 0.08, 0.09, 0.1]$.

which likewise suggests $\gamma = 2/3$. The results clearly follow this scaling, as we see in figure 10(b). Keller & Miksis (1983) likewise reported $\gamma = 2/3$, while Eggers & Dupont (1994), who included viscosity, found that the exponent is weakly time dependent but not far from 2/3.

Finally, of particular interest is the value of $\mathfrak{K}$, and so we ploted $\mathfrak{K} = r_{min}(t_0 - t)^{-2/3}\ We^{1/3}$ in figure 11. Here we see that $\mathfrak{K}$ is independent of r_{min} for much of the period for which (5.1) is satisfied and that the universal constant $\mathfrak{K} = 0.45 \pm 0.025$.

5.2. *Critical Weber number*

The basis for the present study was to explore a possible mechanism by which focused ultrasound can damage the lung. Our hypothesis behind the study is that

https://doi.org/10.1017/S0022112007004648 Published online by Cambridge University Press

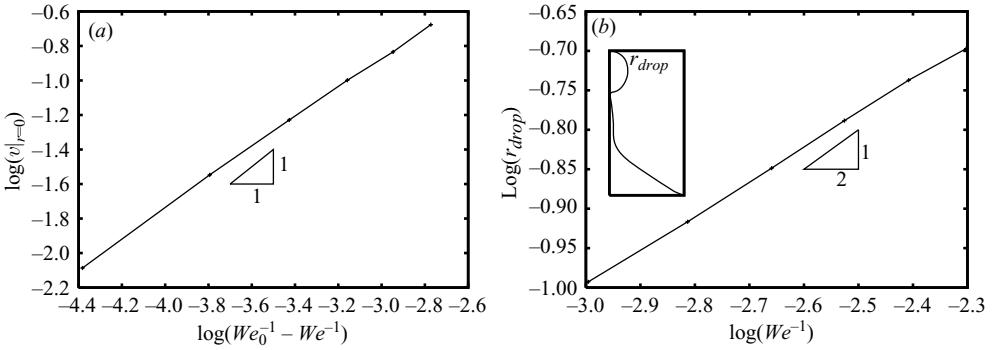


FIGURE 12. Plots of (*a*) $\log(v|_{r=0})$ vs. $\log(We_0^{-1} - We^{-1})$ and (*b*) $\log(r_{drop})$ against $\log(We^{-1})$. The slopes show that the the power-law exponents δ_1 and δ_2 are 1 and 1/2, respectively.

focused ultrasound can act to eject droplets of bodily fluids, which then penetrate the bubble-wrap-like sacs of the lung pleural surface, allowing them to fill with blood. With this premise, an immediate question is whether there exists a particular Weber number which maximizes the amount of energy or momentum imparted to the emitted droplets, so as to effect maximum damage to the pleural surface. To this end, we need to know how the velocity and the size of the emitted droplets depend on the Weber number. Of course the Froude number may too play a role, although as we found earlier it does not have a significant effect on the size of the droplet, so we will for the moment ignore it.

For convenience we use the centreline velocity $v|_{r=0}$ to represent the velocity of the droplets and begin by noting that the cutoff Weber number at which drops are emitted, We_0^{-1}, is by definition the limiting case where the droplet has vanishing velocity. Hence, it is reasonable to postulate that the droplet emission velocity scales as $(We_0^{-1} - We^{-1})^{\delta_1}$, where δ_1 is to be determined.

Of course, in addition to r_{min}, at any time the droplet has a maximum radius, defined in accordance with (5.1), except that now $\mathrm{d}^2r/\mathrm{d}s^2 < 0$. So, as a measure of droplet size we use the maximum radius of the drop, r_{drop} say, when the system reaches the singularity at $t = t_0$. Here too we postulate a power-law relationship between We and r_{drop}, namely $r_{drop} \propto (We^{-1})^{\delta_2}$, where δ_2 is to be determined. By this hypothesis, we are assuming that droplets are formed for all We^{-1} above We_c^{-1} and below We_0^{-1}. That said, we emphasize that it is not clear whether our We_c^{-1}, which is necessary for numerical stability, also credibly measures the physical lower bound at which droplets form or whether the physical value is significantly less than We_c^{-1}. Nevertheless, we obtained the power-law exponents $[\delta_1, \delta_2] = [1, 1/2]$, as presented in figures 12(*a*) and 12(*b*), and thus the following scalings:

$$r_{drop} \sim We^{-1/2} \quad \text{and} \quad v|_{r=0} \sim We_0^{-1} - We^{-1} \quad \text{for} \quad We^{-1} \in \left[We_c^{-1}, We_0^{-1}\right].$$

The fact that r_{drop} increases while $v|_{r=0}$ decreases with We^{-1} suggests the existence of a stationary point where the emitted droplet momentum and energy are maximized or minimized. To expose the existence of these stationary points, we note that momentum and energy scale as follows:

$$\text{momentum} \sim r_{drop}^3 v|_{r=0} \sim \left(\frac{1}{We}\right)^{3/2}\left(\frac{1}{We_0} - \frac{1}{We}\right),$$

https://doi.org/10.1017/S0022112007004648 Published online by Cambridge University Press

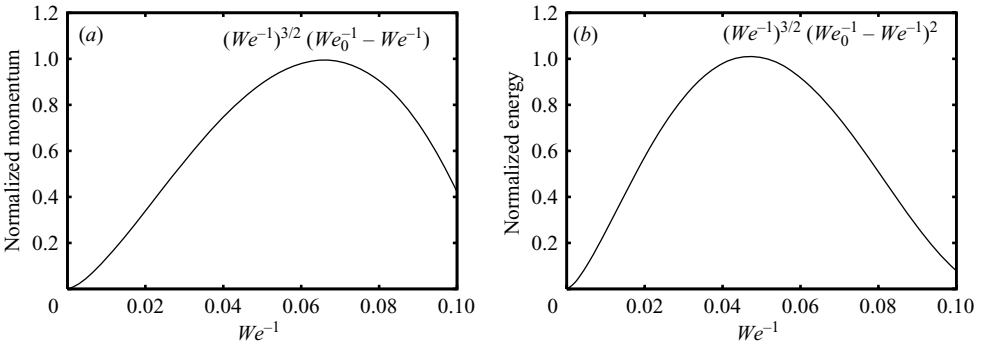


FIGURE 13. Plots of unity-normalized (*a*) drop momentum and (*b*) energy, against the inverse Weber number, We^{-1}.

$$\text{energy} \sim r_{drop}^3 v|_{r=0}^2 \sim \left(\frac{1}{We}\right)^{3/2}\left(\frac{1}{We_0} - \frac{1}{We}\right)^2$$

and plot each in figure 13.

We emphasize that the values for the critical Weber numbers so obtained are not as important as the fact that such critical Weber numbers exist. Furthermore, the particular Weber number that actually maximizes the droplet momentum and droplet energy may depend on other factors, for example, the Froude number. However, while the Froude number does have a direct effect on $v|_{r=0}$, it does not significantly affect the size of the droplet. Therefore, *Fr* can only influence the location of the maximum point in *We* space, not its existence. Avoiding this critical Weber number is crucial to minimizing lung damage.

5.3. *Mechanical index*

Localized peaks in pressure can also play a role in damaging the lung. To that end the US Food and Drug Administration (FDA) sets limits through a dimensional quantity denoted the mechanical index (MI), defined as the estimated peak rarefactional pressure *in vivo* p_r^* (in MPa), divided by the square root of the centre frequency of the acoustic beam, f (in MHz). FDA regulations allow an MI of up to 1.9 for all applications except ophthalic ones, for which the maximum is 0.23. Of interest here, of course, is an estimate of the MI for the mechanism we have studied.

We begin with (2.2) and note that, when the flat free surface is subjected to an impulse in pressure, we have $p_r^* \equiv p_{max}^*$ while $\boldsymbol{u}^* \approx 0$. Then, since p^* is actually the change in bulk pressure owing to the nonlinear interaction of the periodic acoustic pressure evaluated over one acoustic cycle, we have $\Phi = p_r^* T_\lambda/\rho = p_r^*/f\rho$. The physics further requires that the focal zone measured by L be at a minimum comparable with the acoustic wavelength $\lambda = c/f$, so that $Lf/c \geqslant O(1)$ where c is the speed of sound. Thus if we let $L = \mathfrak{h}c/f$ (as in § 1), where $\mathfrak{h} \geqslant O(1)$ is a positive constant, and recall that $We = \Phi^2\rho(L\sigma)^{-1}$ then

$$MI = \frac{p_r^*}{\sqrt{f}} = \mathfrak{h}^{1/2}(\rho\sigma c)^{1/2} We^{1/2}$$

or in nondimensional form

$$\frac{MI}{\mathfrak{h}^{1/2}(\rho\sigma c)^{1/2}} = We^{1/2}. \tag{5.3}$$

https://doi.org/10.1017/S0022112007004648 Published online by Cambridge University Press

Now $c = 1500\,\mathrm{m\,s^{-1}}$ and $\rho = 1059\,\mathrm{kg\,m^{-3}}$ in blood and soft tissue, while $\sigma = 56 \times 10^{-3}\,\mathrm{N\,m^{-1}}$ (in blood), yielding $(\rho\sigma c)^{1/2} \approx 0.3\,\mathrm{MPa\,MHz^{-1/2}}$. So, since gravity is absent in (5.3) and $We^{1/2} \in (3.09, 4.71)$ in the absence of gravity (see § 4.3) then, assuming the smallest admissible value for $\mathfrak{h}$ (≈ 0.3), droplets will be ejected for $MI > 0.5$. Of course the ejection of droplets, even at the critical *We* (Weber number) mentioned in § 5.2, does not guarantee damage to the lung, but it does provide a mechanism for damage, particularly since $\mathfrak{h}$ may well exceed unity.

Appendix A. Admissible φ_0

To determine whether $\varphi(r, \theta, z)$ at $t = 0$ is an admissible solution to (2.1) and the boundary conditions, we require a general solution to (2.1). In building that solution we first note that (2.1) is separable. Next, in order to satisfy the $z \to -\infty$ boundary condition, it is necessary that the solution in z takes the form $\mathrm{e}^{\ell z}$, with $\ell > 0$. Lastly we observe that the radial solution is expressible as a Fourier transform, which, in axisymmetric conditions, reduces to a Hankel transform that necessarily satisfies the $r \to \infty$ boundary condition. The general solution to (2.1) is then

$$\varphi(r, z) = \int_0^\infty \hat{\varphi}(\ell)\ell \mathrm{e}^{\ell z} J_0(\ell r)\,\mathrm{d}\ell, \tag{A 1}$$

where $\hat{\varphi}(\ell)$ can be thought of as a spectrum with wavenumber ℓ and J_0 is the zeroth-order Bessel function of the first kind. To be admissible, therefore, any candidate $\varphi(r, z)$ must be expressible in the form (A 1) or, equivalently, any candidate $\hat{\phi}(\ell)$ that renders (A 1) bounded and everywhere well defined realizes an admissible candidate $\varphi(r, z)$.

On setting $z = 0$, therefore, and assuming (2.10), the inverse Hankel transform indicates that $\hat{\varphi}_0 = \mathrm{e}^{-\ell^2/4}$. Then, on substituting $\hat{\varphi}_0$ back into (A 1) with z now arbitrary, we find that $\varphi(r, z)$ is indeed bounded and everywhere well defined. In short, we are justified in using (2.10).

Appendix B. Asymptotic behaviour

Our intention here is to determine the asymptotic behaviour of the solution. In particular, since the only independent spatial variable in the problem is the surface arclength s, we should like to know how each of the dependent variables r, z and ϕ behaves as $s \to 0$ and $s \to \infty$.

Our starting point is (2.6), where, since z is identically zero at $t = 0$, the integrand vanishes, requiring $\mu|_{t=0} = \mu_0 = 2\phi_0$. Then, for the Gaussian ϕ_0 we have chosen, the initial normal velocity follows analytically as $u_n = \sqrt{\pi} M(3/2, 1, -r^2)$, where M is the confluent hypergeometric function (see e.g. Chapter 13 in Abramovich & Stegun 1965).

Given the impulse velocity field, our task is to integrate forward in time numerically and so the analysis to follow is exact in a time-discretized sense. Then, since $z = 0$ and $r = s$ initially, we find for $t > 0$ but $t \ll 1$ that $z|_{t\ll 1} \approx u_n t + O(t^2)$, at which stage the surface profile is

$$z|_{t\ll 1} \approx \sqrt{\pi} M(3/2, 1, -s^2)t + O(t^2). \tag{B 1}$$

Then, with knowledge of the asymptotic behaviour of M (from Abramovich & Stegun 1965) for small and large values of s, we express each limit as a similar series in which

https://doi.org/10.1017/S0022112007004648 Published online by Cambridge University Press

the coefficients depend upon time, viz.

$$z|_{t\ll 1} \sim \sum_{j=0}^{\infty} \hat{a}_{2j}(t)s^{2j} = \hat{a}_0(t) + \hat{a}_2(t)s^2 + \cdots \qquad \text{as} \quad s \to 0 \tag{B 2}$$

$$z|_{t\ll 1} \sim \sum_{j=1}^{\infty} \hat{b}_{2j+1}(t)\frac{1}{s^{2j+1}} = \hat{b}_3(t)\frac{1}{s^3} + \hat{b}_5(t)\frac{1}{s^5} + \cdots \quad \text{as} \quad s \to \infty. \tag{B 3}$$

Asymptotic expansions for r then follow by requiring that the arc length metric be identically equal to unity, as

$$\left(\frac{dr}{ds}\right)^2 + \left(\frac{dz}{ds}\right)^2 = 1,$$

to yield

$$r|_{t\ll 1} \sim s + \sum_{j=1}^{\infty} \tilde{a}_{2j+1}(t)s^{2+1} = s + \tilde{a}_3(t)s^3 + \cdots \qquad \text{as} \quad s \to 0 \tag{B 4}$$

$$r|_{t\ll 1} \sim s + \tilde{b}_0(t) + \sum_{j=1}^{\infty} \tilde{b}_{2j+5}(t)\frac{1}{s^{2j+5}} = s + \tilde{b}_0(t) + \tilde{b}_7(t)\frac{1}{s^7} + \cdots \quad \text{as} \quad s \to \infty. \tag{B 5}$$

Of interest, however, are expansions for r and z for larger t and these are not quite as (B 2)–(B 5), because of the back effect of the constant of integration $\tilde{b}_0$ on the asymptotic behaviour of z. Physically we can interpret $\tilde{b}_0$ as the 'lengthening' of the fluid surface as it deforms, so $\tilde{b}_0$ is, in general, non-zero. Indeed, since the surface is initially flat, any deformation will increase the total surface arclength. In other words, although $r \to \infty$ as $s \to \infty$, the constant $\tilde{b}_0 = \lim_{s\to\infty}[r(s) - s] \neq 0$. The effect of $\tilde{b}_0$ becomes significant in subsequent time steps as it cascades through the evolution equations, producing negative even powers of s (in addition to the previous odd powers) in the asymptotic expansion for z for large s. This in turn modulates the behaviour of r at large s, because r and z are related via the arclength metric.

Thus for $t = O(1)$ and large s we have

$$\left.\begin{aligned} z &\sim \sum_{j=3}^{\infty} \hat{b}_j(t)\frac{1}{s^j} = \hat{b}_3(t)\frac{1}{s^3} + \hat{b}_4(t)\frac{1}{s^4} + \cdots \qquad \text{as} \quad s \to \infty \\ r &\sim s + \tilde{b}_0(t) + \sum_{j=7}^{\infty} \tilde{b}_j(t)\frac{1}{s^j} = s + \tilde{b}_0(t) + \tilde{b}_7(t)\frac{1}{s^7} + \tilde{b}_8(t)\frac{1}{s^8} + \cdots \quad \text{as} \quad s \to \infty, \end{aligned}\right\} \tag{B 6}$$

while the behaviour as $s \to 0$ remains unchanged.

We should like to thank Hyuck Chung, William O'Brien, James Zachary and the late John Harris for their interest and helpful discussions. This work was supported by the National Institutes of Health of the USA, grant R01-EB02641 (formerly HL58218).

REFERENCES

ABRAMOVICH, M. & STEGUN, I. A. 1965 *Handbook of Mathematical Functions*, 3rd Edn. Dover.

https://doi.org/10.1017/S0022112007004648 Published online by Cambridge University Press

BAKER, G. R., MEIRON, D. I. & ORSZAG, S. A. 1984 Boundary integral methods for axistmmetric and three-dimensional Rayleigh-Taylor instability problems. *Physica* **12D**, 19–31.

BASARAN, O. A. 2002 Small-scale free surface flows with breakup: Drop formation and emerging applications. *AICHE J.* **48**, 1842–1848.

BRENNER, M. P., EGGERS, J., JOSEPH, K., NAGEL, S. R. & SHI, X. D. 1997 Breakdown of scaling in droplet fission at high Reynolds number. *Phys. Fluids* **9**, 1573–1590.

BRENNER, M. P., LISTER, J. R. & STONE, H. A. 1996 Pinching threads, singularities and the number 0.0304... *Phys. Fluids* **8**, 2827–2836.

CHILD, S. Z., HARTMAN, C. L., SCHERY, L. A. & CARTENSEN, E. L. 1990 Lung damage from exposure to pulsed ultrasound. *Ultrasound Med. Biol.* **16**, 817–825.

CINBIS, C., MANSOUR, N. N. & KHURI-YAKUB, B. T. 1993 Effect of surface tension on the acoustic radiation pressure-induced motion of the water-air interface. *J. Acoust. Soc. Am.* **94**, 2365–2372.

DAY, R. F., HINCH, E. J. & LISTER, J. R. 1998 Self-similar capillary pinchioff of an inviscid fluid. *Phys. Rev. Lett.* **80**, 704–707.

DOMMERMUTH, D. G. & YUE, D. K. P. 1987 Numerical simulations of nonlinear axisymmetrical flows with a free surface. *J. Fluid Mech.* **178**, 195–219.

EGGERS, J. 1993 Universal pinching of 3d axisymmetric free-surface flow. *Phys. Rev. Lett.* **71**, 3458–3460.

EGGERS, J. & DUPONT, T. F. 1994 Drop formation in a one-dimensional approximation of the Navier-Stokes equation. *J. Fluid Mech.* **262**, 205–221.

ELROD, S. A., HADIMIOGLU, B., KHURI-YAKUB, B. T., RAWSON, E., RICHLEY, E., MANSOUR, N. N. & LUNDGREN, T. S. 1989 Nozzleless droplet formation with focused accoustic beam. *J. Appl. Phys.* **65**, 3441–3447.

FARADAY, M. 1831 On the forms and states assumed by fluids in contact with vibrating elastic surfaces. *Phil. Trans. R. Soc.* **52**, 319–340.

FORNBERG, B. 1996 *A Practical Guide to Pseudospectral Methods*, 1st Edn. Cambridge University Press.

HARRISON, G. H., EDDY, H. A., WAND, J.-P. & LIBERMAN, F. Z. 1995 Microscopic lung alterations and reduction of respiration rate in insonated anesthetized swine. *Ultrasound Med. Biol.* **21**, 981–983.

HARTMAN, C. L., CHILD, S. Z., MAYER, R., SCHENK, E. & CARTENSEN, E. L. 1990 Lung damage from exposure to fields of an electrohydraulic lithotripter. *Ultrasound Med. Biol.* **16**, 675–683.

HOLLAND, C. K., DENG, C. X., APFEL, R. E., ALDERMAN, J. L. & FERNANDEZ, L. A. 1996 Direct evidence of cavitation in vivo from diagnostic ultrasound. *Ultrasound Med. Biol.* **22**, 917–925.

HOU, T. Y., LOWENGRUB, J. S. & SHELLEY, M. J. 1994 Removing the stiffness from interfacial flows with surface tension. *J. Comput. Phys.* **114**, 312–338.

HOU, T. Y., LOWENGRUB, J. S. & SHELLEY, M. J. 1997 The long-time motion of vortex sheets with surface tension. *Phys. Fluids* **9**, 1933–1954.

HOU, T. Y., LOWENGRUB, J. S. & SHELLEY, M. J. 2001 Boundary integral methods for multicomponent fluids and multiphase materials. *J. Comput. Phys.* **169**, 302–362.

JAMES, A. J., SMITH, M. K. & GLEZER, A. 2003 Vibration-induced drop atomization and the numerical simulation of low-frequency single-droplet ejection. *J. Fluid Mech.* **476**, 29–62.

JASWON, M. A. & SYMM, G. T. 1977 *Integral Equation Methods in Potential Theory and Electrostatics*, 1st Edn. Academic.

KELLER, J. B. & MIKSIS, M. J. 1983 Surface tension driven flows. *SIAM J. Appl. Maths* **43**, 268–277.

KINO, G. S. 1987 *Accoustic Waves:Devices, Imaging and Analog Signal Processing*, 1st Edn. Prentice-Hall.

LANG, R. J. 1962 Ultrasonic atomization of liquids. *J. Acoust. Soc. Am.* **34**, 6–8.

LEPPINEN, D. & LISTER, J. R. 2003 Capillary pinch-off in inviscid fluids. *Phys. Fluids* **15**, 568–578.

LIN, S. P. & REITZ, R. D. 1998 Drop and spray formation from a liquid jet. *Annu. Rev. Fluid Mech.* **20**, 85–105.

https://doi.org/10.1017/S0022112007004648 Published online by Cambridge University Press

LUNDGREN, T. S. & MANSOUR, N. N. 1988 Oscillations of drops in zero gravity with weak viscous effect. *J. Fluid Mech.* **194**, 479–510.

MONIKA, N. & STEEN, P. H. 2004 Numerical simulations of inviscid capillary pinchoff. *J. Comp. Physut.* **200**, 299–324.

MOORE, D. W. 1976 The stability of an evolving two-dimensional vortex sheet. *Mathematika* **23**, 35–44.

MOORE, D. W. 1979 The spontaneous appearance of a singularity in the shape of an evolving vortex sheet. *Proc. R. Soc. Lond.* A **365**, 105–119.

NIE, Q. 2001 The nonlinear evolution of vortex sheets with surface tension in axisymmetric flows. *J. Comput. Phys.* **174**, 438–459.

NIE, Q. & BAKER, G. 1998 Application of adaptive quadrature to axi-symmetric vortex sheet motion. *J. Comput. Phys.* **143**, 49–69.

PEREGRINE, D. H., SHOKER, G. & SYMON, A. 1990 The bifurcation of liquid bridges. *J. Fluid Mech.* **212**, 25–39.

PHILLIPS, W. R. C. & WU, Z. 1994 On the instability of wave-catalysed longitudinal vortices in strong shear. *J. Fluid Mech.* **272**, 235–254.

PULLIN, D. I. 1982 Numerical studies of surface-tension effects in nonlinear Kelvin-Helmholtz and Rayleigh-Taylor instability. *J. Fluid Mech.* **119**, 507–532.

SCHULKES, R. M. S. M. 1994 The evolution and bifurcation of a pendant drop. *J. Fluid Mech.* **278**, 83–100.

TARANTAL, A. F. & CANFIELD, D. R. 1994 Ultrasound-induced lung haemorrhage in the monkey. *Ultrasound Med. Biol.* **20**, 65–72.

WIKES, E. D., PHILLIPS, S. D. & BASARAN, O. A. 1999 Computational and experimental analysis of dynamics of drop formation. *Phys. Fluids* **11**, 3577–3598.

WOOD, W. R. & LOOMIS, A. L. 1927 The physical and biological effects of high frequency sound-waves of great intensity. *Phil. Mag.* **4**, 417–437.

YOUNG, T. 1805 An essay on the cohesion of fluids. *Phil. Trans. R. Soc. Lond.* **95**, 65–87.

ZACHARY, J., FRIZZELL, L., ABBOTT, J., DUNN, F. & SANGHVI, N. 2000*a* Selected biological properties of tissues: Potential determinants of susceptibility of ultrasound-induced bioeffects. *J. Ultrasound Med.* **19**, 85–96.

ZACHARY, J. F. & O'BRIEN, W. D. 1995 Lung lesions induced by continuous- and pulsed-wave(diagnostic) ultrasound in mice, rabbits, and pigs. *Vet. Pathol.* **32**, 43–54.

ZACHARY, J. F., O'BRIEN, W. D., FRIZZEL, L. A. & WEIGEL, R. M. 2000*b* Ultrasound-induced lung haemorrhage is not caused by inertial cavitation. *J. Acoust. Soc. Am.* **108**, 1290–1297.

https://doi.org/10.1017/S0022112007004648 Published online by Cambridge University Press